molecules

MDPI

*Article*

# Solvent and Substituent Size Influence on the Cyclochiral Rigidity of Aminomethylene Derivatives of Resorcin[4]arene

**Waldemar Iwanek**

Faculty of Chemical Technology and Engineering, Bydgoszcz University of Technology, Seminaryjna 3, 85-326 Bydgoszcz, Poland; waldemar.iwanek@pbs.edu.pl

**Abstract:** Resorcin[4]arenes (R[4]A) are a group of macrocyclic compounds whose peculiar feature is the presence of eight hydroxyl groups in their structure. The directional formation of intramolecular hydrogen bonds with their participation leads to the formation of a cyclochiral racemic mixture of these compounds. Their stability strongly depends on the substituent and especially the environment in which they are located. The paper discusses the cyclochiral nature of aminomethylene derivatives of R[4]A (AMD-R[4]A). Their cyclochiral rigidity in non-polar solvents has been shown. The influence of the size of the alkyl groups in the amino substituents of AMD-R[4]A on their cyclochiral nature was noted. To calculate the reaction paths for their racemization, the nudged elastic band (NEB) method was employed using the semi-empirical DFT (GFN1-xTB) approach. The calculated activation barrier energies for their racemization in chloroform, obtained through various semi-empirical quantum chemical methods (SE), Hartree–Fock (HF), and density functionals theory (DFT), show good correlation with experimental observations. Among the tested methods, the B38LYP-D4 method is highly recommended due to its fast computational speed and accuracy, which is comparable to the time-consuming double-hybrid DH-revDSD-PBEP86 approach.

**Keywords:** resorcin[4]arene; cyclochiral; reaction path; DFT calculations



**Citation:** Iwanek, W. Solvent and Substituent Size Influence on the Cyclochiral Rigidity of Aminomethylene Derivatives of Resorcin[4]arene. *Molecules* **2023**, *28*, 7426. https://doi.org/10.3390/molecules28217426

Academic Editor: Gheorghe Dan Pantoș

Received: 24 September 2023
Revised: 26 October 2023
Accepted: 30 October 2023
Published: 4 November 2023



## 1. Introduction

R[4]A is a type of macrocyclic compound that exhibits stability in its upper rim and crown conformation, which is achieved through a system of intramolecular hydrogen bonds [1]. The strength of these hydrogen bonds and their interactions depend greatly on the polarity and nature of the surrounding environment (solvent). For instance, in chloroform, R[4]A molecules undergo self-assembly into hexamers and octamers [2]. Similar self-assembly behavior has also been observed in toluene [3]. The unique characteristics of these supramolecules, such as their internal closed cavity and distinct electron solvation properties, have sparked interest in studying chemical reactions that can occur within them [4]. The "*ortho*" positions in R[4]A are particularly reactive and can be utilized for modifying the upper rim through processes like the Mannich reaction [5]. This enables the synthesis of aminomethylene derivatives of R[4]A with high yields, utilizing formaldehyde and primary or secondary amines [6,7], amino alcohols, and amino acids [8,9]. These compounds possess intriguing receptor properties towards various organic and biological compounds, making them of interest in different fields [10,11].

On the topic of the derivatives mentioned, the existing literature lacks studies demonstrating a significant relationship between their structure and the polarity/nature of the solvent, as well as the size of the amino groups. This research aims to address this gap by highlighting the cyclochiral nature of these derivatives in non-polar solvents, along with their pronounced stabilization when using amines with branched alkyl groups. Theoretical calculations were conducted to determine the energy barriers associated with the racemization of enantiomers of these derivatives, and the mechanisms involved were thoroughly discussed.

The discussed AMD-R[4]A molecules contain 150–200 atoms in their structure, and as a result of this, DFT calculations are very time-consuming, especially geometry optimization and accurate determination of energy. Moreover, dispersion effects, as the particle size increases, play an increasingly important role in both geometry optimization and accurate energy calculations. In the literature, there is no assessment of SE and DFT methods in relation to R[4]A and its derivatives in terms of the assessment of reaction energy, the height of reaction barriers, or non-covalent interactions. For this reason, the author decided to test several SE methods most frequently used in the literature (PM6-D3H4 [12], GFN2-xTB [13], and AIQM1 [14]), the HF-D3-ACP method [15] due to its parameterization in the field of thermochemistry and reaction barriers, and fast DFT-3c composite methods (B97-3c [16], r2scan-3c [17], PBEh-3c [18]), as well as several DFT methods for calculating reaction barriers, i.e., B38LYP-D4 [19], M062X [20], wB97M-V [21], and DH-revDSD-PBEP86-D4 [22].

## 2. Results and Discussion

AMD-R[4]A derivatives were synthesized through the Mannich reaction of R[4]A with formaldehyde and various secondary amines in ethanol. The secondary amines used include N,N-dimethylamine (**1**), N,N-diethylamine (**2**), N,N-dipropylamine (**3**), N,N-diisopropylamine (**4**), pyrrolidine (**5**), piperidine (**6**), morpholine (**7**), and N-methylpiperazine (**8**). These derivatives are stabilized by a system of eight intramolecular hydrogen bonds in non-polar environments. Their directionality (*M*, *P*) affects the generation of stereogenic centers (*S* or *R*) on the methine carbons connecting the resorcinol rings in R[4]A. Figure 1 illustrates the structures of the described AMD-R[4]A molecules, with the lower part of the figure symbolically representing their cyclochirality. The color green represents the lower rim with stereogenic centers, while purple represents the hydrogen bonds in the upper rim of AMD-R[4]A. The symbols *M* and *P* indicate the direction of the hydrogen bonds, which ultimately determine the enantiomers of these compounds.

The NMR spectra of AMD-R[4]A exhibit notable variations when recorded in solvents of varying proton donor–acceptor properties and polarity. Figure 2 illustrates an example of the 1H and 13C NMR spectra of derivative **2**, obtained in $CDCl_3$ and acetone-$d_6$ solvents.

In chloroform (Figure 2A), we observe diastereotopic methylene protons -$CH_2$- (a) in the form of slightly fuzzy doublets and diastereotopic methylene protons (b) in the lower rim of the derivative **2**. This phenomenon arises from the directional rigidity of the upper rim, which is caused by a strong hydrogen bond forming between the amino group and the adjacent hydroxyl group proton (d) in the resorcinol ring ($Et_2N\cdots$HO-Ph). This feature of these compounds determines their cyclochirality. The NMR spectrum also reveals two types of hydrogen bonding within the chemical shift range of d = 8–14 ppm. One of them was mentioned above, the second type of hydrogen bonding (c) between the hydroxyl groups of the resorcinol rings (Ph-HO$\cdots$HO-Ph) that stabilizes the crown conformation of derivative **2**. The cyclochiral rigidity and directional arrangement of the amino groups can also be observed in the 13C NMR spectrum. This is reflected in the different chemical shifts of carbons e and e′ (153.1 and 150.6 ppm, respectively) and f, f′ (124.1 and 123.9 ppm) of resorcinol rings as well as carbons g, g′ (23.1, 22.9 ppm) of methyl groups ($CH_3$) in the lower rim of the derivative **2**.

In the presence of acetone (Figure 2B), it can be observed that all the protons discussed in the 1H NMR spectrum, as well as the carbon atoms in the 13C NMR spectrum, appear as singlets. Additionally, the hydroxyl group protons are observed as an extended singlet, exhibiting a chemical shift value of d = 8.67 ppm. This can be attributed to the strong solvation of the derivative **2** in acetone, which probably results in the breaking of intramolecular hydrogen bonds of the amino group with the hydroxyl group in favor of the formation of intermolecular hydrogen bonds of the hydroxyl groups with the oxygen atom of the acetone molecule.

Molecule **2** becomes even more rigid in non-polar solvents such as $CCl_4$ and benzene (Figure 2C). In these solvents, for methylene protons (a), we observe a doublet of doublets, characteristic of cyclic rigid structures such as oxazine or boron derivatives of R[4]A [23,24].

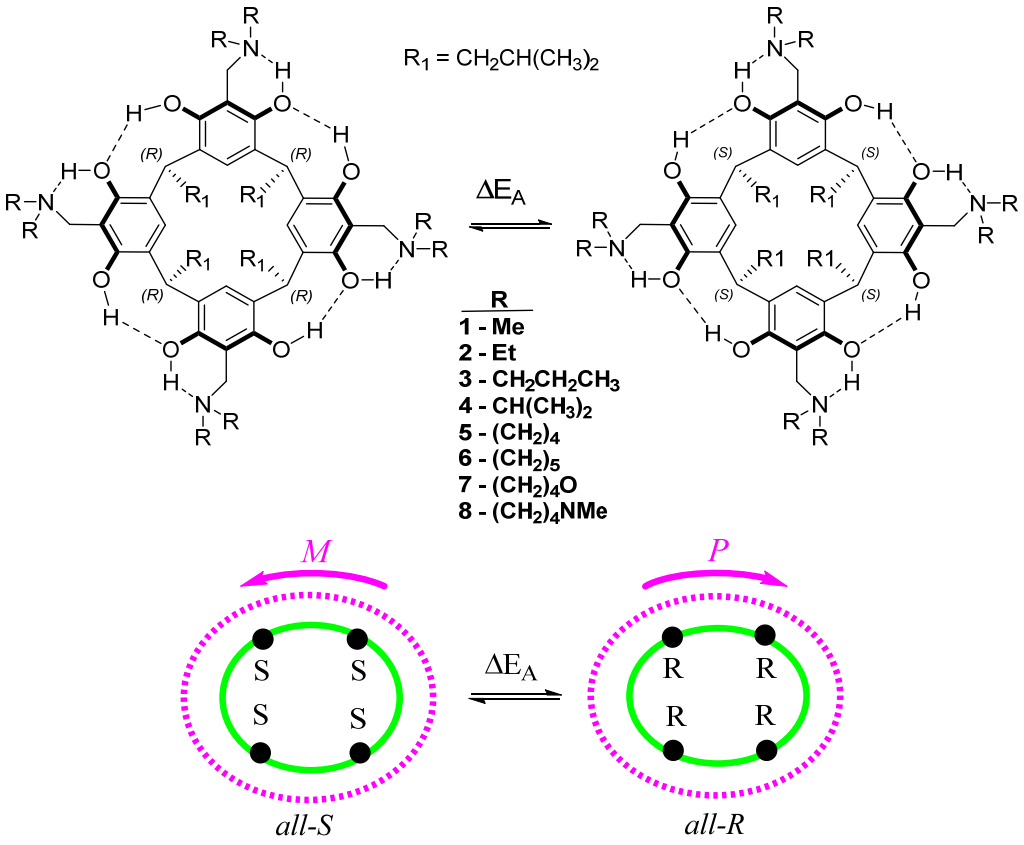


**Figure 1.** The structure of the cyclochiral AMD-R[4]A with a schematic picture of the cyclochiral nature of these derivatives. The color green represents the lower rim with stereogenic centers, while purple represents the hydrogen bonds in the upper rim of AMD-R[4]A. The symbols *M* and *P* indicate the direction of the hydrogen bonds, which ultimately determine the enantiomers of these compounds.

It was also observed that AMD-R[4]A derivatives exhibit cyclochiral stiffness, which becomes more pronounced with the increasing size of the alkyl groups on the amino substituents. In the chloroform NMR spectrum, derivative **3** with a dipropylamino group displays a classically resolved doublet of proton doublets for the methylene group (a) (Figure 2D). This proves the special rigidity of this structure in this solvent, which is also confirmed by the 13C NMR spectrum and separated signals of carbons e, e′ and f, f′. Additional fragments of the 1H and 13C NMR spectra for derivatives **2**, **4**, and **6** are presented, depicting the methylene group -$CH_2$- (a) and the chemical shifts of carbon atoms (e, e′ and f, f′). Conversely, the remaining AMD-R[4]A derivatives exhibit an extended singlet of protons for the methylene group and strongly broadened signals for the e, e′ and f, f′ carbons (see Supplementary Materials). Given the rigid cyclochiral structure of derivatives **2**, **3**, **4**, and **6** in non-polar solvents, several intriguing questions arise: How stable are these structures in chloroform? What is the racemization barrier for these compounds, and what is the accompanying racemization mechanism? To answer these questions, the NEB method [25] was used to obtain saddle points (SP) and intermediate state point (IS) as well as minimum energy paths between known initial (*M*-AMD-R[4]A) and final states (*P*-AMD-R[4]A). Optimization of the geometry of the generated structures along the reaction path in $CHCl_3$ was carried out using the fast semi-empirical DFT method—GFN1-xTB [26] in $CHCl_3$ with the analytical linearized Poisson–Boltzmann (ALPB) solvent model [27]. The SP and IS structures obtained by this method were further subjected to geometrical optimization using the DFT B97-3c method to determine the transition states (TS), intermediate state (IS), substrate (S), and product (P) structures, utilizing the conductor-like polarizable continuum model (CPCM) solvent model [28] for chloroform.

Frequency calculations were then performed to confirm one imaginary and appropriate frequency for each TS, while no imaginary frequency for all local minima. The optimized geometrical structures were then employed for single-point energy (SPE) calculations in chloroform, employing semi-empirical (SE) methods, the Hartree–Fock method (HF-D3), and DFT methods with the universal solvation model (SMD) [29] for HF and DFT methods. For the SE methods, SPE calculations were performed using suitable solvent models: PM6-D3H4/COSMO, GFN2-xTB/ALPB, and AIQM1 in the gas phase. Scheme 1 illustrates the procedure for optimizing the geometry and conducting single-point energy calculations for individual structures.

The NEB/GFN1-xTB method generated a reaction path for derivative **1** in $CHCl_3$, depicted in Figure 3. The path consists of 43 images, with the highest points representing the geometrical structures SP, and the lowest point representing the geometrical structure IS. The optimized structures of these points, indicated in red, are displayed above and below the energy change curve, as seen in the figure. As the curve shows, it is evident that the racemization reaction of *M*-AMD-R[4]A to *P*-AMD-R[4]A occurs in two steps and involves a non-chiral intermediate state (IS).

The SP and IS structures found by this method served as input structures for geometric optimization by the DFT B97-3c method of the TS and IS structures and subsequent calculations of the activation energy of the racemization reaction ($\Delta E_A{}^F$) and the activation energy of the back reaction ($\Delta E_A{}^B$). Figure 4 visually represents these energy values and also showcases the $CHCl_3$-optimized structures of TS and IS for derivative **1** obtained through the B97-3c calculations.

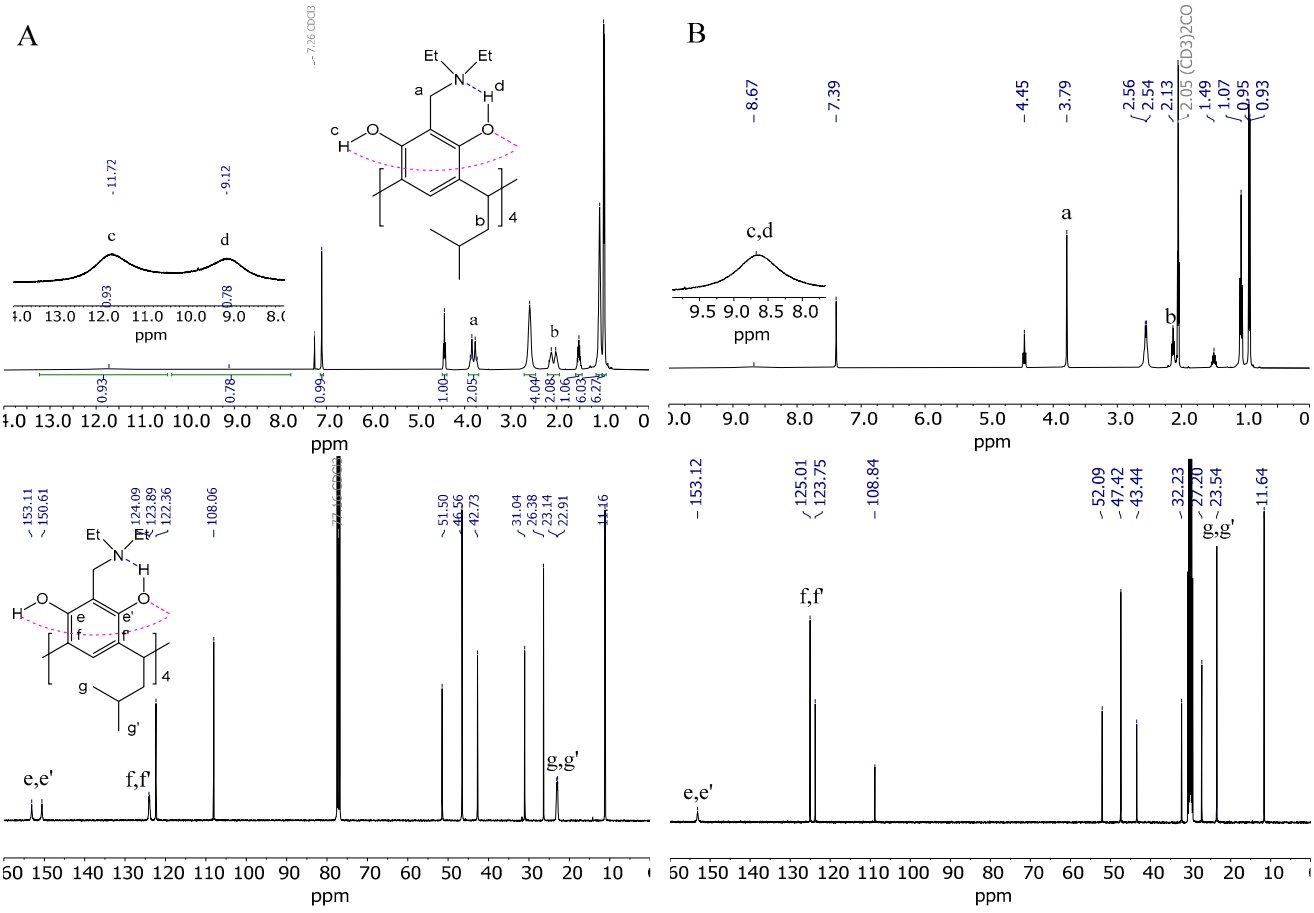


**Figure 2.** *Cont.*

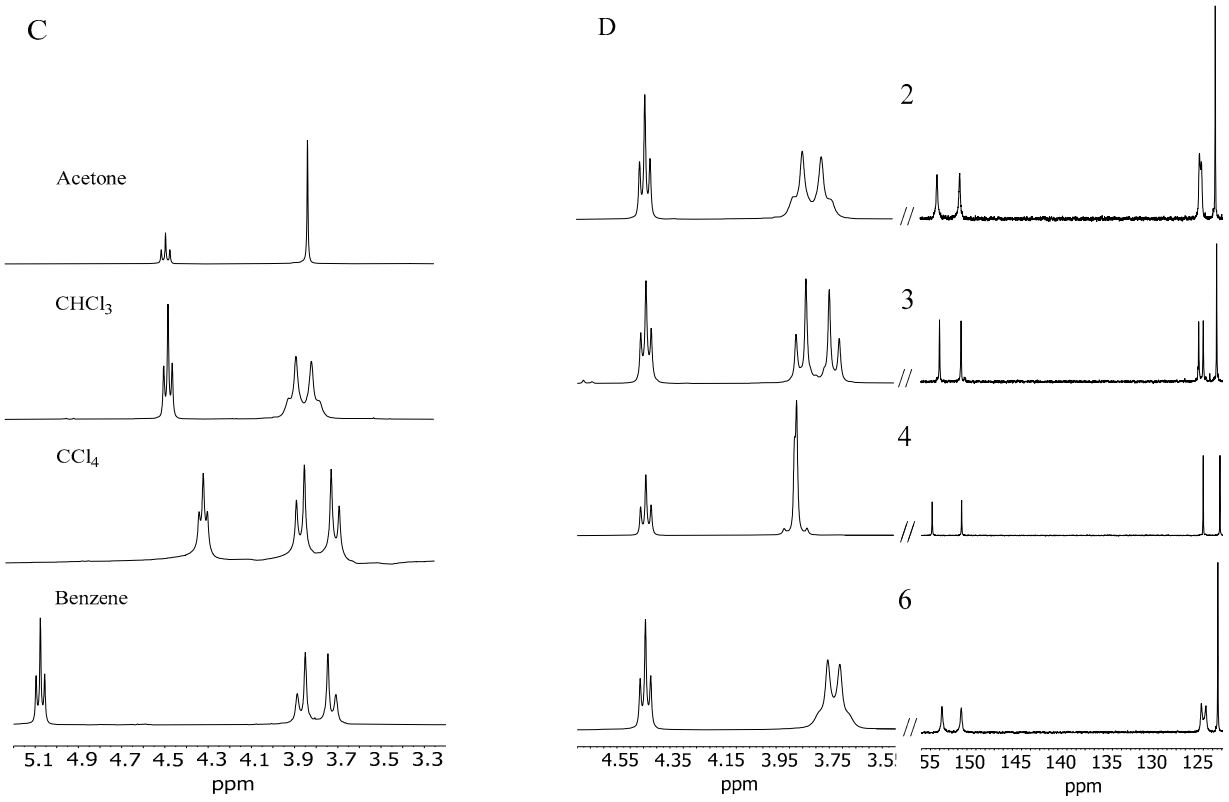


**Figure 2.** (**A**) 1H and 13C NMR spectrum of derivative **2** in $CHCl_3$; (**B**) 1H and 13C NMR spectrum of derivative **2** in acetone; (**C**) spin–spin coupling comparison of the methylene group (a) derivative **2** in acetone, $CHCl_3$, $CCl_4$, and benzene; (**D**) comparison of fragments of 1H and 13C NMR spectra in $CHCl_3$ of AMD-R[4]A derivatives: **2**, **3**, **4**, **6**, respectively.

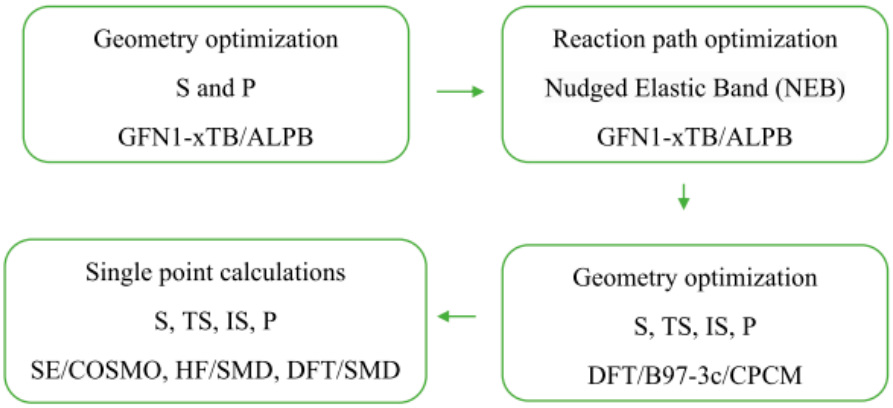


**Scheme 1.** Procedure used for geometry optimization and one-point energy calculations of substrates (S), transition states (TS), intermediate states (IS), and products (P) of AMD-R[4]A racemization reaction.

Theoretical calculations have confirmed that the structures of the $TS_1$ and $TS_2$ states exhibit mirror symmetry, and the orientation of the hydrogen bond in the transition state aligns with that of the initial states. In transition states, only intramolecular hydrogen bonds between hydroxyl groups are preserved, while intramolecular hydrogen bonds between amino groups and hydroxyl groups are not observed. In the intermediate state (IS), hydrogen bonds are reorganized, and hydrogen bonds are formed between the hydroxyl groups of two opposite resorcinol units with adjacent resorcinol units. Additionally, intramolecular hydrogen bonds form between the amino groups and hydroxyl groups in the

opposing resorcinol units, resulting in a structure with a plane of symmetry, as indicated by the dotted blue line in Figure 4.

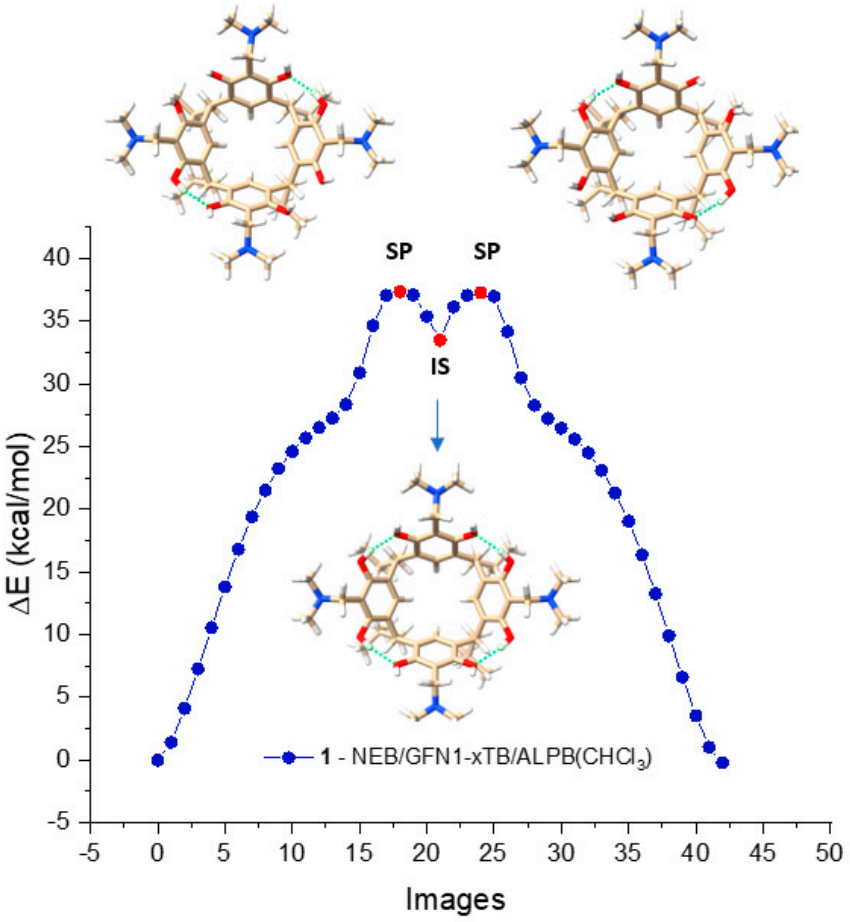


**Figure 3.** Racemization reaction path of derivative **1** in $CHCl_3$ calculated by NEB/xTB1 presented in the form of 43 geometrically optimized images. The images marked in red represent the structures of the saddle points (SP) and the intermediate state (IS) point.

Table 1 presents the activation energies ($\Delta E_A{}^F$ and $\Delta E_A{}^B$) in kcal/mol for AMD-R[4]A derivatives. The calculations were performed using selected HF methods and DFT on geometries obtained from the B97-3c method. The activation energies determined with the B38LYP-D4 method were found to be closest to the reference values obtained from the DH-revDSD-PBEP86-D4 double-hybrid functional. The largest absolute error of this method for the racemization activation energy $\Delta E_A{}^F$ = 0.82 kcal/mol was found for derivative **4**, while for the activation energy of the back reaction $\Delta E_A{}^B$ = 0.44 kcal/mol, this was found for derivative **3**. It is worth noting that the B38LYP calculations were significantly faster, approximately twenty times faster, compared to the double-hybrid method when performed with the same number of processors. Similarly, the DFT method using the r2scan-3c functional was approximately sixty times faster than the double-hybrid method. For this method, the largest absolute deviations from the reference values were as follows: $\Delta E_A{}^F$ = 3.28 kcal/mol for derivative **6** and $\Delta E_A{}^B$ = 0.82 kcal/mol for derivative **7**. In turn, calculations using the M062X functional gave the largest deviations $\Delta E_A{}^B$ = 3.78 kcal/mol and $\Delta E_A{}^B$ = 1.27 kcal/mol for derivative **4**.

The HF-D3/6-31G(d)-ACP method, which employs a specially trained 6-31G(d)-ACP basis for thermochemical calculations and energy barrier height determination, has proven to be competitive. Notably, calculations using this method are significantly faster than those using a double-hybrid approach. The largest discrepancies in activation energy calculations were observed for derivative **2**, with values of $\Delta E_A{}^F$ = 3.36 kcal/mol and

$\Delta E_A{}^B$ = 1.98 kcal/mol. In contrast, the discrepancies for the other derivatives were much smaller compared to the reference values.

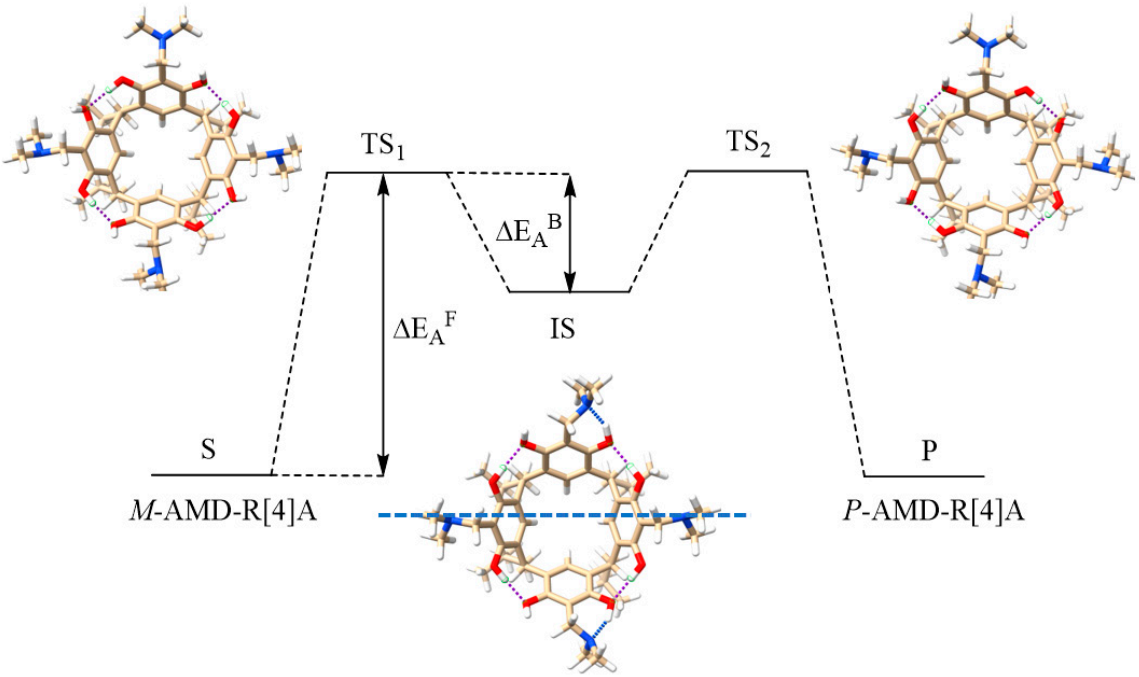


**Figure 4.** Activation energies of $\Delta E_A{}^F$ racemization and back reaction $\Delta E_A{}^B$ along with geometrically optimized by B97-3c method in $CHCl_3$ structures of $TS_1$, $TS_2$, and IS for derivative **1**.

Among the SE methods listed in Table 2, the AIQM1 method exhibits results that closely resemble the double-hybrid method, even though the calculations were performed in the gas phase. The maximum error obtained using AIQM1 was $\Delta E_A{}^F$ = 3.10 kcal/mol for derivative **7** and $\Delta E_A{}^B$ = 4.82 kcal/mol for derivative **4**. In the case of the PM6-D3H4 and GFN2-xTB methods, significant discrepancies were observed for both activation energies in comparison to the reference values.

In order to better visualize the obtained results, deviations from the reference values are presented in Figure 5 in the form of a bar graph of the data contained in Tables 1 and 2.

The calculations presented in this study align with the experimentally observed trend of increased stiffness in AMD-R[4]A molecules as the alkyl groups of the amino substituents become more branched. The activation energy barriers for racemization increase from derivative **1** through derivative **2** and **3** to derivative **4**, with values of $\Delta E_A{}^F$ (kcal/mol) as follows: 33.59, 37.63, 38.87, and 41.26. This trend is also reflected in the 1H and 13C NMR spectra, where extended signals of diastereotopic -$CH_2$- protons and separated signals of carbon atoms bound to hydroxyl groups (e, e′) are observed. Derivatives **5** and **6** contain cyclic amines in their structure, pyrrolidine and piperidine, respectively. Their two closest carbon atoms to the nitrogen atom are at a similar distance as in derivative **1** ($NMe_2$ group). The remaining carbon atoms are significantly distant from the aromatic part of R[4]A, which results in very small dispersion interactions. This is probably the reason for the comparable values of their activation energies $\Delta E_A{}^F$ (kcal/mol) for the derivatives: **1** = 33.59; **5** = 33.35; **6** = 34.33. Surprisingly low barriers to racemization activation and the back reaction were found for the morpholine derivative **7**, with values of $\Delta E_A{}^F$ = 15.94 kcal/mol and $\Delta E_A{}^F$ = 5.11 kcal/mol. Similarly, for derivative **8**, which also contains nitrogen in the cyclic amino group, the calculated activation barriers are lower compared to amino substituents without heteroatoms. This suggests a preliminary conclusion that the presence of a heteroatom in a cyclic secondary amine reduces the activation energy of cyclochiral racemization for such derivatives, as well as the barrier for the back reaction.

**Table 1.** Activation energies $\Delta E_A^F$ and $\Delta E_A^B$ (kcal/mol) for AMD-R[4]A derivatives, respectively, calculated using selected HF and DFT methods on geometries calculated using the B97-3c method. The reference values obtained with the DH-revDSD-PBEP86-D4 method are marked in blue, the B38LYP-D4 method recommended for calculations in violet.

| AMD-R[4]A/ΔE | | HF-D3-ACP | B97-3c | r2scan-3c | PBEh-3c | B38LYP-D4 | M062X | wB97M-V | DH-revDSD-PBEP86-D4 |
|---|---|---|---|---|---|---|---|---|---|
| **1** | $\Delta E_A^F$ | 32.11 | 38.53 | 35.60 | 39.65 | 33.53 | 36.28 | 31.52 | 33.59 |
| | $\Delta E_A^B$ | 14.83 | 16.80 | 15.75 | 16.69 | 14.68 | 15.32 | 13.70 | 15.06 |
| **2** | $\Delta E_A^F$ | 34.27 | 42.74 | 39.02 | 41.63 | 37.50 | 38.19 | 34.45 | 37.63 |
| | $\Delta E_A^B$ | 13.39 | 17.49 | 15.73 | 15.59 | 15.31 | 15.13 | 13.69 | 15.37 |
| **3** | $\Delta E_A^F$ | 35.68 | 43.04 | 39.58 | 41.34 | 38.27 | 39.10 | 34.89 | 38.87 |
| | $\Delta E_A^B$ | 18.36 | 21.19 | 19.84 | 19.58 | 19.28 | 19.14 | 17.40 | 19.72 |
| **4** | $\Delta E_A^F$ | 38.82 | 46.77 | 43.42 | 45.92 | 42.08 | 45.04 | 39.28 | 41.26 |
| | $\Delta E_A^B$ | 14.63 | 17.78 | 16.35 | 17.20 | 16.15 | 17.37 | 14.45 | 16.10 |
| **5** | $\Delta E_A^F$ | 32.81 | 38.55 | 34.85 | 39.86 | 34.14 | 35.88 | 31.34 | 33.35 |
| | $\Delta E_A^B$ | 15.00 | 16.80 | 14.96 | 16.46 | 15.32 | 15.09 | 13.69 | 14.98 |
| **6** | $\Delta E_A^F$ | 33.70 | 40.42 | 37.61 | 41.53 | 34.75 | 36.94 | 32.20 | 34.33 |
| | $\Delta E_A^B$ | 22.96 | 24.21 | 23.00 | 25.05 | 22.23 | 22.26 | 20.67 | 22.13 |
| **7** | $\Delta E_A^F$ | 15.66 | 18.64 | 16.96 | 19.32 | 16.53 | 17.43 | 15.01 | 15.94 |
| | $\Delta E_A^B$ | 6.25 | 4.26 | 4.29 | 4.54 | 5.41 | 4.05 | 4.79 | 5.11 |
| **8** | $\Delta E_A^F$ | 23.44 | 28.48 | 26.12 | 29.37 | 24.34 | 25.80 | 22.43 | 23.93 |
| | $\Delta E_A^B$ | 13.31 | 13.21 | 12.60 | 13.60 | 12.52 | 11.85 | 11.50 | 12.42 |

**Table 2.** Activation energies $\Delta E_A^F$ and $\Delta E_A^B$ (kcal/mol) for AMD-R[4]A derivatives, respectively, calculated with selected SE methods on geometries calculated with the B97-3c method.

| AMD-R[4]A/ΔE | | PM6-D3H4 | GFN2-xTB | AIQM1 |
|---|---|---|---|---|
| **1** | $\Delta E_A^F$ | 31.73 | 28.52 | 33.48 |
| | $\Delta E_A^B$ | 12.84 | 10.01 | 11.80 |
| **2** | $\Delta E_A^F$ | 29.88 | 28.08 | 38.28 |
| | $\Delta E_A^B$ | 13.22 | 9.39 | 12.60 |
| **3** | $\Delta E_A^F$ | 33.02 | 32.03 | 37.03 |
| | $\Delta E_A^B$ | 16.39 | 15.52 | 16.79 |
| **4** | $\Delta E_A^F$ | 46.18 | 34.36 | 40.78 |
| | $\Delta E_A^B$ | 18.56 | 9.21 | 11.28 |
| **5** | $\Delta E_A^F$ | 32.21 | 29.15 | 35.16 |
| | $\Delta E_A^B$ | 11.25 | 10.53 | 13.83 |
| **6** | $\Delta E_A^F$ | 38.69 | 31.18 | 36.52 |
| | $\Delta E_A^B$ | 14.49 | 13.30 | 18.80 |
| **7** | $\Delta E_A^F$ | 18,83 | 14.32 | 18.87 |
| | $\Delta E_A^B$ | 2.23 | 1.15 | 2.02 |
| **8** | $\Delta E_A^F$ | 27.36 | 21.73 | 27.03 |
| | $\Delta E_A^B$ | 4.56 | 4.90 | 9.78 |

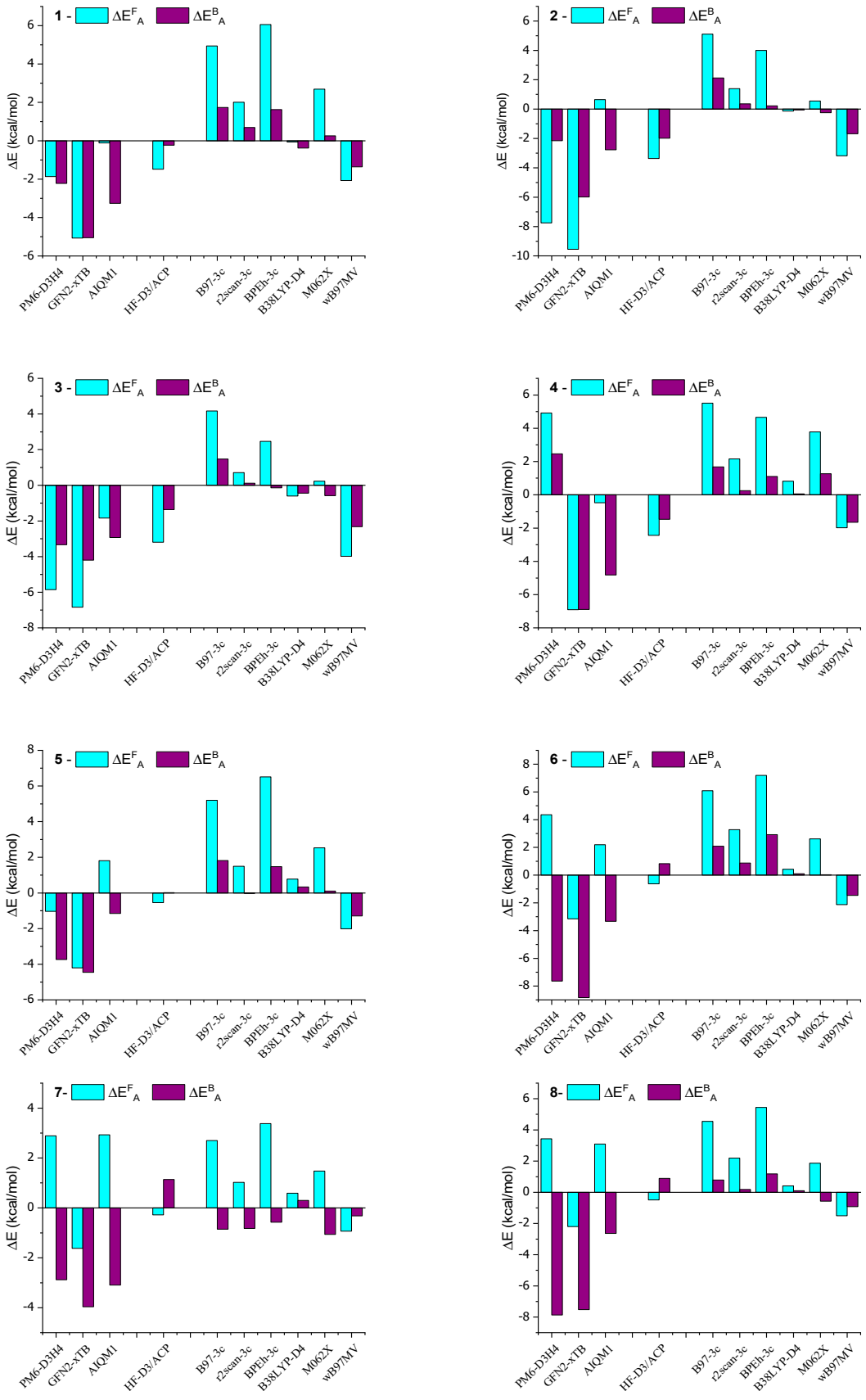


**Figure 5.** Bar chart of relative deviations (kcal/mol) from reference values obtained using the DH−revDSD−PBEP86−D4 functional for the data in Tables 1 and 2.

Experimental findings (Figure 2C) reveal that molecule **2** exhibits increased rigidity in non-polar solvents such as benzene and $CCl_4$ compared to $CHCl_3$. This observation was further supported by calculations using the B38LYP-D4 method, which determined the height of the racemization barriers ($\Delta E_A{}^F$) in benzene and $CCl_4$ using the SMD solvent model. The calculated racemization activation energies are: in benzene $\Delta E_A{}^F$ = 42.69 kcal/mol, in $CCl_4$ $\Delta E_A{}^F$ = 42.64 kcal/mol, and are more than 5.1 kcal/mol higher than the activation barrier in $CHCl_3$ ($\Delta E_A{}^F$= 37.50 kcal/mol). However, we do not observe practically any change in the activation energy of the back reaction, which for benzene and $CCl_4$ are $\Delta E_A{}^B$= 15.36 kcal/mol and $\Delta E_A{}^B$ = 15.26 kcal/mol, respectively, while for $CHCl_3$ it is $\Delta E_A{}^B$ = 15.31 kcal/mol.

The observed significant decrease in rigidness in acetone can likely be attributed to the increased involvement of the hydroxyl groups of molecule **2** in the formation of hydrogen bonds with polar acetone molecules, as opposed to hydrogen bonding with the nitrogen atom of amino groups. Thus, the change in the hydrogen bond system from intramolecular (non-polar solvents) to intermolecular (polar solvents containing heteroatoms) is responsible for the substantial reduction in the activation energy barrier for cyclochiral racemization of the studied derivatives.

## 3. Experimental Section

The NMR spectra were achieved using an Avance 400 ultra-shield spectrometer (Bruker, Karlsruhe, Germany). Reagents and solvents were obtained from Fluka (Buchs, Switzerland), and Merck (Darmstad, Germany) and were used without purification.

*Calculation procedure*: All NEB and DFT calculations were performed with the ORCA 5.0.3 and 5.04 software package [30] with default setting. For the B97-3c, r2scan-3c, and PBEh-3c methods, built-in base sets were used for calculations. For the M062X functionals, the 6-311G(d,p) basis was used, for the wB97M-V, the def2-TZVP basis. In the case of the B38LYP-D4 functional, the def2-mTZVP base and the D4 dispersion parameters from work [19] were used. Calculations with the DH-revDSDPBEP86-D4 functional were carried out with the def2-TZVPP basis recommended in [22] and the D4 dispersion parameters. The HF-D3-ACP calculations were performed with Gaussian 16 software packages [31] with 6-31G(d)-ACP basis and D3 dispersion parameters as in work [15]. GFN1-xTB calculations were performed with the development version xtb v. 6.5.0 [32]. The PM6-D3H4 were conducted with the MOPAC program version 21.237W [33]. The AIQM1 calculations were performed online on the MLatom@XACS cloud service [34].

*AMD-R[4]A synthesis procedure:* A total of 0.2 g (0.225 mmol) of R[4]A was weighed into a round-bottomed flask and dissolved in 10 mL of ethanol. Then 5 equivalents of formaldehyde and 5 equivalents of sec-amine were added and left at room temperature for 24 h. The precipitate was then filtered, washed with cold ethanol, and dried. The yields of AMD-R[4]A derivatives formation ranged from 66% to 85%.

*15,35,55,75-tetrakis((dimethylamino)methyl)-2,4,6,8-tetraisobutyl-1,3,5,7(1,3)-tetrabenzena-cyclooctaphan-14,16,34,36,54,56,74,76-octaol* (**1**), (66% yield), white solid. $^1$H NMR (400 MHz, $CDCl_3$, T = 298 K) δ [ppm]: 8.68 (br. s., 8H, OH), 7.11 (s, 4H, PhH), 4.43 (t, *J* = 7.70 Hz, 4H, CH), 3.71 (s, 8H, $CH_2$), 2.29 (s, 24H, $CH_3$), 2.07 (m, 8H, $CH_2$), 1.51 (m, 4H, CH), 0.97 (d, *J* = 6.60 Hz, 24H $CH_3$); $^{13}$C NMR (100 MHz, $CHCl_3$, T = 298 K) δ [ppm]: 152.4, 150.8, 124.0, 122.5, 108.2, 56.9, 44.5, 42.9, 31.1, 26.4, 23.0.

*15,35,55,75-tetrakis((diethylamino)methyl)-2,4,6,8-tetraisobutyl-1,3,5,7(1,3)-tetrabenzena-cyclooctaphan-14,16,34,36,54,56,74,76-octaol* (**2**), (72% yield), white solid. $^1$H NMR (400 MHz, $CDCl_3$, T = 298 K) δ [ppm]: 11.85 (br.s., 4H, OH), 9.15 (br.s., 4H OH), 7.10 (s, 4H, PhH), 4.44 (t, *J* = 7.70 Hz, 4H, CH), 3.81(dd, *J* = 14.30 Hz, 8H, $CH_2$), 2.59 (br. s., 16H, $CH_2$), 2.12 (m, 4H, $CH_2$), 2.02(m, 4H, $CH_2$), 1.52 (m, 4H, CH), 1.07 (br. s., 24H, $CH_3$), 0.97 (d, *J* = 6.60 Hz, 24H, $CH_3$); $^{13}$C NMR (100 MHz, $CHCl_3$, T = 298 K) δ [ppm]: 152.9, 150.4, 123.9, 123.7, 122.2, 107.9, 51.3, 46.4, 42.6, 30.9, 26.2, 23.0, 22.7, 11.0.

*15,35,55,75-tetrakis((diprophylamino)methyl)-2,4,6,8-tetraisobutyl-1,3,5,7(1,3)-tetrabenzena-cyclo-octaphan-14,16,34,36,54,56,74,76-octaol* (**3**), (68% yield), white solid. $^{1}$H NMR (400 MHz, $CDCl_3$, T = 298 K) δ [ppm]: 11.45 (br. s., 4H, OH), 8.86 (br.s., 4H, OH), 7.12 (s, 4H, PhH), 4.44 (t, *J* = 7.70 Hz, 4H, CH), 3.79 (dd, *J* = 14.30 Hz, 8H, $CH_2$), 2.45 (br.s., 16H, $CH_2$), 2.15 (m, 4H, $CH_2$), 2.00 (m, 4H, $CH_2$), 1.52 (m, 20H, CH, $CH_2$), 0.97 (t, *J* = 5.87 Hz, 24H, $CH_3$), 0.87 (t, *J* = 6.97 Hz, 24H, $CH_3$); $^{13}$C NMR (100 MHz, $CHCl_3$, T = 298 K) δ [ppm]: 152.9, 150.5, 124.3, 123.8, 122.3, 108.2, 55.7, 52.9, 42.8, 31.0, 26.3, 23.2, 22.8, 19.6, 11.9.

*15,35,55,75-tetrakis((diisoprophylamino)methyl)-2,4,6,8-tetraisobutyl-1,3,5,7(1,3)-tetra-benzena-cyclooctaphan-14,16,34,36,54,56,74,76-octaol* (**4**), (68% yield), white solid. $^{1}$H NMR (400 MHz, $CDCl_3$, T = 298 K) δ [ppm]: 9.24 (s, 4H, OH), 7.05 (s, 4H, PhH), 4.44 (t, *J* = 7.70 Hz, 4H, CH), 3.87 (dd, *J* = 16.40 Hz, 8H, $CH_2$), 3.18, br. s., 4H, CH), 3.05 (br. s., 4H, CH), 2.10 (m, 4H, $CH_2$), 2.00 (m, 4H, CH), 1.52 (m, 4H, CH), 1.18 (br. s., 12H, $CH_3$), 1.11 (br. s., 12H, $CH_3$), 1.02 (br. s., 24H, $CH_3$), 0.96 (m, 24H, $CH_3$); $^{13}$C NMR (100 MHz, $CHCl_3$, T = 298 K) δ [ppm]: 153.8, 150.6, 123.8, 122.0, 116.5, 108.2, 48.7, 43.3, 42.6, 30.9, 26.3, 23.2, 22.8, 20.7, 19.2.

*15,35,55,75-tetrakis((pirrolidin)methyl)-2,4,6,8-tetraisobutyl-1,3,5,7(1,3)-tetrabenzenacyclo-octaphan-14,16,34,36,54,56,74,76-octaol* (**5**), (74% yield), white solid. $^{1}$H NMR (400 MHz, $CDCl_3$, T = 298 K) δ [ppm]: 9.73 (s, 8H, OH), 7.12 (s, 4H, PhH), 4.46 (t, *J* = 7.70 Hz, 4H, CH), 3.90 (s, 8H, $CH_2$), 2.66 (br. s., 16H, $CH_2$), 2.10 (br. s., 8H, $CH_2$), 1.84 (s, 16H, $CH_2$), 1.54 (m, 4H, CH), 1.00 (d, *J* = 6.60 Hz, 24H, $CH_3$); $^{13}$C NMR (100 MHz, $CHCl_3$, T = 298 K) δ [ppm]: 152.8, 150.1, 124.0, 122.3, 108.7, 53.7, 53.1, 42.7, 31.1, 26.4, 23.8, 23.0.

*15,35,55,75-tetrakis((piperidin)methyl)-2,4,6,8-tetraisobutyl-1,3,5,7(1,3)-tetrabenzenacyclo-octaphan-14,16,34,36,54,56,74,76-octaol* (**6**), (74% yield), white solid. $^{1}$H NMR (400 MHz, $CDCl_3$, T = 298 K) δ [ppm]: 11.98 (br.s., 4H, OH), 9.00 (br.s., 4H, OH), 7.10 (s, 4H, PhH), 4.44 (t, *J* = 7.70 Hz, 4H, CH), 3.73 (br. q., 8H, $CH_2$), 2.91 (br. s., 8H, $CH_2$), 2.12 (br.s., 8H, $CH_2$), 2.02 (br. s., 8H, $CH_2$), 1.60 (br. s., 24H, $CH_2$), 1.52 (m, 4H, CH), 0.97 (d, *J* = 6.60 Hz, 24H, $CH_3$); $^{13}$C NMR (100 MHz, $CHCl_3$, T = 298 K) δ [ppm]: 152.6, 150.4, 124.1, 123.6, 122.3, 107.6, 55.9, 53.7, 42.6, 30.9, 26.2, 25.6, 23.9, 23.0, 22.7.

*15,35,55,75-tetrakis((morpholin)methyl)-2,4,6,8-tetraisobutyl-1,3,5,7(1,3)-tetrabenzenacyclo-octaphan-14,16,34,36,54,56,74,76-octaol* (**7**), (85% yield), white solid. $^{1}$H NMR (400 MHz, $CDCl_3$, T = 298 K) δ [ppm]: 8.87 (br. s., 8H, OH), 7.11 (s, 4H, PhH), 4.42 (t, *J* = 7.70 Hz, 4H, CH), 3.73 (m, 24H, $CH_2$), 2.52 (br. s., 16H, $CH_2$), 2.06 (s, 8H, $CH_2$), 1.49 (m, 4H, CH), 0.97 (d, *J* = 6.60 Hz, 24H, $CH_3$); $^{13}$C NMR (100 MHz, $CHCl_3$, T = 298 K) δ [ppm]: 151.4, 124.0, 122.9, 107.4, 66.8, 55.5, 52.9, 42.7, 31.1, 26.4, 23.0.

*15,35,55,75-tetrakis((4-methylpiperazin)methyl)-2,4,6,8-tetraisobutyl-1,3,5,7(1,3)-tetra-benzenacy-clooctaphan-14,16,34,36,54,56,74,76-octaol* (**6**), (71% yield), white solid. $^{1}$H NMR (400 MHz, $CDCl_3$, T = 298 K) δ [ppm]: 8.31 (br. s., 8H, OH), 7.10 (s, 4H, PhH), 4.42 (t, *J* = 7.70 Hz, 4H, CH), 3.77 (s, 8H, $CH_2$), 2.70 (br. s., 32H, $CH_2$), 2.30 (s, 12H, $CH_3$), 2.06 (br. s., 8H, $CH_2$), 1.49 (m, 4H, CH), 0.97 (d, *J* = 6.60 Hz, 24H, $CH_3$); $^{13}$C NMR (100 MHz, $CHCl_3$, T = 298 K) δ [ppm]: 152.1, 150.7, 124.3, 123.7, 122.6, 107.6, 55.1, 54.8, 52.5, 46.0, 42.7, 31.0, 26.3, 23.0.

## 4. Conclusions

The article investigates the impact of solvent polarity and the size of the amino groups on the cyclochiral behavior of AMD-R[4]A. They display increased rigidity of R[4]A cyclic systems. Furthermore, it was noted that amino substituents with branched amino groups, such as derivatives **3** and **4**, already exhibit rigidity similar to cyclic systems, even in $CHCl_3$. On the other hand, in polar solvents such as acetone, AMD-R[4]A derivatives do not show rigidity at room temperature.

The *M–P* racemization reaction paths of AMD-R[4]A derivatives were calculated using the NEB/GFN1-xTB/ALPB($CHCl_3$) method, and the activation energies accompanying

this reaction were calculated using selected SE, HF, and DFT methods. The structures of the *P* and *M* enantiomers and the TS and IS states were optimized by DFT B97-3c in $CHCl_3$. The activation energies calculated by the double-hybrid method DH-revDSD-PBEP86-D4 in $CHCl_3$ using the SMD solvent model were used as reference values. The calculated activation energies for amino substituents without heteroatoms in the cyclic correlate well with the experimentally observed rigidity of those derivatives for which the activation energy of the racemization reaction increases in the series from derivative **1** to **4**. Theoretical confirmation is also supported by the observation that cyclochiral rigidity increases with decreasing solvent polarity.

The obtained results allow for a better understanding of the cyclochiral nature of DMA-R[4]A derivatives and draw attention to this process in relation to other R[4]A derivatives. At the same time, the obtained results confirm that changing the nature of the solvent and its polarity has a significant impact on the behavior of R[4]A derivative molecules. The development in recent years of rapid potential energy screening methods allows for a better understanding of reaction paths (for example racemization) and reaction mechanisms involving these compounds.

**Supplementary Materials:** The following supporting information can be downloaded at: https://www.mdpi.com/article/10.3390/molecules28217426/s1, Supplementary Materials File for full experimental data: NMR spectra of AMD-R[4]A and coordinates of the optimized structures in $CHCl_3$.

**Funding:** This research was funded by Bydgoszcz University of Technology/Poland (BN-WTiICh-3/2023) and Wroclaw Centre for Networking and Supercomputing/Poland (grant no. 27538605).

**Data Availability Statement:** All experimental data and calculations are provided in the Supplementary Materials.

**Conflicts of Interest:** The author declare no conflict of interest.

## References

1. Timmerman, P.; Verboom, W.; Reinhoudt, D.N. Resorcinarenes. *Tetrahedron* **1996**, *52*, 2663–2704. [CrossRef]
2. Horin, I.; Slovak, S.; Cohen, Y.J. Diffusion NMR Reveals the Structures of the Molecular Aggregates of Resorcin[4]arenes and Pyrogallol [4] arenes in Aromatic and Chlorinated Solvents. *Phys. Chem. Lett.* **2022**, *13*, 10666–10670. [CrossRef] [PubMed]
3. Fujii, S.; Sakurai, K. Structural Analysis of an Octameric Resorcinarene Self-Assembly in Toluene and its Morphological Transition by Temperature. *J. Phys. Chem. Lett.* **2021**, *12*, 6464–6468. [CrossRef] [PubMed]
4. Zhang, Q.; Catti, L.; Tiefenbacher, K. Catalysis inside the Hexameric Resorcinarene Capsule. *Acc. Chem. Res.* **2018**, *51*, 2107–2114. [CrossRef]
5. Mannich, C.; Krösche, W. Ueber ein kondensationsprodukt aus formaldehyd, ammoniak und antipyrin. *Arch. Pharm.* **1912**, *250*, 647–667. [CrossRef]
6. Iwanek, W.; Mattay, J. Chiral calixarenes derived from resorcinol. *Liebigs Ann.* **1995**, *8*, 1463–1466. [CrossRef]
7. Matsushita, Y.; Matsui, T. Synthesis of aminomethylated calix [4] resorcinarenes. *Tetrahedron Lett.* **1993**, *34*, 7433–7436. [CrossRef]
8. Iwanek, W.; Wolff, C.; Mattay, J. Chiral calixarenes derived from resorcinol II. Functionalization by mannich reaction with α-aminoalcohols. *Tetrahedron Lett.* **1995**, *36*, 8969–8972. [CrossRef]
9. Wzorek, A.; Mattay, J.; Iwanek, W. Synthesis and structural investigation of the cyclochiral boron resorcinarenes obtained from L-amino acids and phenylboronic acid. *Tetrahedron Asymmet.* **2012**, *23*, 271–277. [CrossRef]
10. Hoskins, C.; Papachristou, A.; Ho, T.M.H.; Hine, J.; Curtis, A.D.M. Investigation into Drug Solubilisation Potential of Sulfonated Calix[4] resorcinarenes. *J. Nanomed. Nanotechnol.* **2016**, *7*, 3–7.
11. Zappacosta, R.; Aschi, M.; Ammazzalorso, A.; Di Profio, P.; Fontana, A.; Siani, G. Embedding calix [4] resorcinarenes in liposomes: Experimental and computational investigation of the effect of resorcinarene inclusion on liposome properties and stability. *BBA Biomembr.* **2019**, *1861*, 1252–1259. [CrossRef]
12. Rezac, J.; Hobza, P. Advanced Corrections of Hydrogen Bonding and Dispersion for Semiempirical Quantum Mechanical Methods. *J. Chem. Theory Comput.* **2012**, *8*, 141–151. [CrossRef] [PubMed]
13. Bannwarth, C.; Ehlert, S.; Grimme, S. GFN2-xTB—An Accurate and Broadly Parametrized Self-Consistent Tight-Binding Quantum Chemical Method with Multipole Electrostatics and Density-Dependent Dispersion Contributions. *J. Chem. Theory Comput.* **2019**, *15*, 1652–1671. [CrossRef] [PubMed]
14. Chen, Y.; Ou, Y.; Zheng, P.; Huang, Y.; Ge, F.; Dral, P.O. Benchmark of general-purpose machine learning-based quantum mechanical method AIQM1 on reaction barrier heights. *J. Chem. Phys.* **2023**, *21*, 074103. [CrossRef]

15. Prasad, V.K.; Otero-de-la-Roza, A.; Di Labio, G.A. Fast and Accurate Quantum Mechanical Modeling of Large Molecular Systems Using Small Basis Set Hartree−Fock Methods Corrected with Atom-Centered Potentials. *J. Chem. Theory Comput.* **2022**, *18*, 2208–2232. [CrossRef] [PubMed]
16. Brandenburg, J.G.; Bannwarth, C.; Hansen, A.; Grimme, S. B97-3c: A revised low-cost variant of the B97-D density functional method. *J. Chem. Phys.* **2018**, *148*, 064104. [CrossRef]
17. Grimme, S.; Hansen, A.; Ehlert, S.; Mewes, J.M. r2SCAN-3c: A "Swiss army knife" composite electronic-structure method. *J. Chem. Phys.* **2021**, *154*, 064103. [CrossRef] [PubMed]
18. Grimme, S.; Brandenburg, J.G.; Bannwarth, C.; Hansen, A. Consistent structures and interactions by density functional theory with small atomic orbital basis sets. *J. Chem. Phys.* **2015**, *143*, 054107. [CrossRef]
19. Santra, G.; Martin, J.M.L. What Types of Chemical Problems Benefit from Density-Corrected DFT? A Probe Using an Extensive and Chemically Diverse Test Suite. *J. Chem. Theory Comput.* **2021**, *17*, 1368–1379. [CrossRef]
20. Zhao, Y.; Truhlar, D.G. The M06 suite of density functionals for main group thermochemistry, thermochemical kinetics, noncovalent interactions, excited states, and transition elements: Two new functionals and systematic testing of four M06-class functionals and 12 other functionals. *Theor. Chem. Acc.* **2008**, *120*, 215–241.
21. Mardirossian, N.; Head-Gordon, M. ωB97M-V: A combinatorially optimized, range-separated hybrid, meta-GGA density functional with VV10 nonlocal correlation. *J. Chem. Phys.* **2016**, *144*, 214110. [CrossRef] [PubMed]
22. Santra, G.; Sylvetsky, N.; Martin, J.M.L. Minimally Empirical Double-Hybrid Functionals Trained against the GMTKN55 Database: RevDSD-PBEP86-D4, revDOD-PBE-D4, and DOD-SCAN-D4. *J. Phys. Chem. A* **2019**, *123*, 5129–5143. [CrossRef] [PubMed]
23. Iwanek, W. Chiral calixarene derived from resorcinol. Part 4: Diastereoselective closure of the oxazine ring. *Tetrahedron Asymmet.* **1998**, *9*, 4289–4290. [CrossRef]
24. Iwanek, W.; Fröhlich, R.; Schwab, P.; Schurig, V. The synthesis and crystallographic structures of novel bora-oxazino-oxazolidine derivatives of resorcarene. *Chem. Commun.* **2002**, *8*, 2516–2517. [CrossRef]
25. Henkelman, G.; Jonsson, H. Improved tangent estimate in the nudged elastic band method for finding minimum energy paths and saddle points. *J. Chem. Phys.* **2000**, *113*, 9978–9985. [CrossRef]
26. Grimme, S.; Bannwarth, C.; Shushkov, P. A Robust and Accurate Tight-Binding Quantum Chemical Method for Structures, Vibrational Frequencies, and Noncovalent Interactions of Large Molecular Systems Parameterized for All spd-Block Elements (Z = 1–86). *J. Chem. Theory Comput.* **2017**, *13*, 1989–2009. [CrossRef]
27. Ehlert, S.; Stahn, M.; Spicher, S.; Grimme, S. Robust and Efficient Implicit Solvation Model for Fast Semiempirical Methods. *J. Chem. Theory Comput.* **2021**, *17*, 4250–4261. [CrossRef]
28. Barone, V.; Cossi, M. Quantum Calculation of Molecular Energies and Energy Gradients in Solution by a Conductor Solvent Model. *J. Phys. Chem. A* **1998**, *102*, 1995–2001. [CrossRef]
29. Marenich, A.V.; Cramer, C.J.; Truhlar, D.G. Universal Solvation Model Based on Solute Electron Density and on a Continuum Model of the Solvent Defined by the Bulk Dielectric Constant and Atomic Surface Tensions. *J. Phys. Chem. B* **2009**, *113*, 6378–6396. [CrossRef]
30. Nesse, F. Software update: The ORCA program system—Version 5.0 WIREs. *Comput. Mol. Sci.* **2022**, *12*, e1606. [CrossRef]
31. Frisch, M.J.; Trucks, G.W.; Schlegel, H.B.; Scuseria, G.E.; Robb, M.A.; Cheeseman, J.R.; Scalmani, G.; Barone, V.; Petersson, G.A.; Nakatsuji, H.; et al. *Gaussian 16, Wersja C.01*; Gaussian, Inc.: Wallingford, CT, USA, 2016.
32. Semiempirical Extended Tight-Binding Program Package xtb Version 6.50. Available online: https://github.com/grimme-lab/xtb (accessed on 15 May 2022).
33. James, J.; Stewart, P. *MOPAC2016 (Version: 21.237W)*; Stewart Computational Chemistry: Kolorado Springs, CO, USA, 2016; Available online: http://OpenMOPAC.net (accessed on 1 March 2023).
34. Mlatom@XACS Cloud Computing Service. Available online: https://xacs.xmu.edu.cn/ (accessed on 5 June 2023).